JGR Solid Earth

RESEARCH ARTICLE
10.1029/2019JB017419

Key Points:
- GPS data show no interseismic slip on Hilina fault system (HFS) during 2001–2017
- InSAR shows subcentimeter HFS offsets in the 4 May 2018 M6.9 earthquake
- A new fault scarp formed on eastern end of the HFS during and after the earthquake

Supporting Information:
- Supporting Information S1

Correspondence to:
K. Wang,
kwang@seismo.berkeley.edu

Citation:
Wang, K., MacArthur, H. S., Johanson, I., Montgomery-Brown, E. K., Poland, M. P., Cannon, E. C., et al. (2019). Interseismic quiescence and triggered slip of active normal faults of Kīlauea Volcano's south flank during 2001–2018. *Journal of Geophysical Research: Solid Earth*, *124*, 9780–9794. https://doi.org/10.1029/2019JB017419

Received 23 JAN 2019
Accepted 11 AUG 2019
Accepted article online 16 AUG 2019
Published online 3 SEP 2019

Interseismic Quiescence and Triggered Slip of Active Normal Faults of Kīlauea Volcano's South Flank During 2001–2018

K. Wang[1], H. S. MacArthur[2], I. Johanson[3], E. K. Montgomery-Brown[4], M. P. Poland[5], E. C. Cannon[6], M. A. d'Alessio[7], and R. Bürgmann[1]

[1]Department of Earth and Planetary Sciences, University of California, Berkeley, CA, USA, [2]Seismological Laboratory, California Institute of Technology, Pasadena, CA, USA, [3]Hawaiian Volcano Observatory, U.S. Geological Survey, Hawaii National Park, HI, USA, [4]California Volcano Observatory, U.S. Geological Survey, Menlo Park, CA, USA, [5]Cascades Volcano Observatory, U.S. Geological Survey, Vancouver, WA, USA, [6]Golder Associates Inc., Anchorage, AK, USA, [7]Department of Geological Sciences, California State University Northridge, Northridge, CA, USA

Abstract The mobile south flank of Kīlauea Volcano hosts two normal fault systems, the Koa'e fault system (KFS) and the Hilina fault system (HFS). In historical time, at least three M>6.5 earthquakes have occurred on the basal detachment of the Kīlauea Volcano's south flank, with the most recent being the 4 May 2018 M6.9 earthquake. Here we analyze kinematic Global Positioning System data collected from 2001 to 2017 and interferometric synthetic aperture radar data before, during, and after the 2018 M6.9 earthquake to determine the crustal motion across the HFS and KFS faults. Our results indicate that the HFS faults did not significantly slip during the interseismic period from 2007 to 2011. Despite its substantial magnitude, interferometric synthetic aperture radar (InSAR) data show that the 2018 M6.9 earthquake triggered subcentimeter level slip along sections of the previously mapped HFS branches. Up to 20 cm of offset occurred on what appears to be a newly formed (or previously unknown) fault near the eastern end of the HFS. During the 3 months following the M6.9 earthquake, up to ~30 cm of slip occurred along the KFS, which helps accommodate rapid large-scale subsidence of Kīlauea's summit region as large volumes of summit reservoir magma fed the lower East Rift Zone eruption. The HFS appears to activate only in concert with large earthquakes on the basal detachment. The KFS, on the other hand, moves both seismically during small local earthquakes and aseismically in response to nearby earthquakes and caldera subsidence.

1. Introduction

The south flank of Kīlauea, an active volcano on the south side of the Island of Hawai'i (Figure 1), moves seaward at rates of up to 10 cm/year along a subhorizontal basal detachment fault rooted at 8- to 10-km depth (Ando, 1979; Borgia et al., 2000; Owen et al., 1995; Owen et al., 2000). The mobile south flank is bounded by the Koa'e fault system (KFS), and the Kīlauea's Southwest and East Rift Zones (ERZ), which accommodate continuous deep rift expansion, episodic shallow rift intrusions, and associated eruptions (Figure 1). The volcano is built on a weak layer of pelagic sediments (Swanson et al., 1976; Dieterich, 1988; Delaney et al., 1990), which is a mobile interface accommodating the stress accumulated from dike emplacement and gravitational instability of the edifice. In addition to continuous detachment creep (e.g., Owen et al., 2000), episodic slow slip events (e.g., Brooks et al., 2008; Montgomery-Brown et al., 2015) and infrequent large-magnitude earthquakes (e.g., Owen & Bürgmann, 2006) also carry the flank seaward. The three largest recorded detachment earthquakes were the 1868 M ~7.9 Great Ka'u (e.g., Wyss, 1988), 1975 M 7.7 Kalapana (e.g., Ando, 1979; Owen & Bürgmann, 2006), and 4 May 2018 M 6.9 earthquakes (Neal et al., 2018).

The edifice itself hosts two major normal fault systems, the Koa'e fault system (KFS) and the Hilina fault system (HFS). The KFS is a series of mostly north facing normal faults immediately south (seaward) of the summit caldera that run between the Southwest and East Rift Zones with scarps up to 15-m high (Duffield, 1975). We note that both north and south facing faults are found in the KFS. The age of these faults is probably much older than what their scarp heights imply because they are growth faults that have been frequently

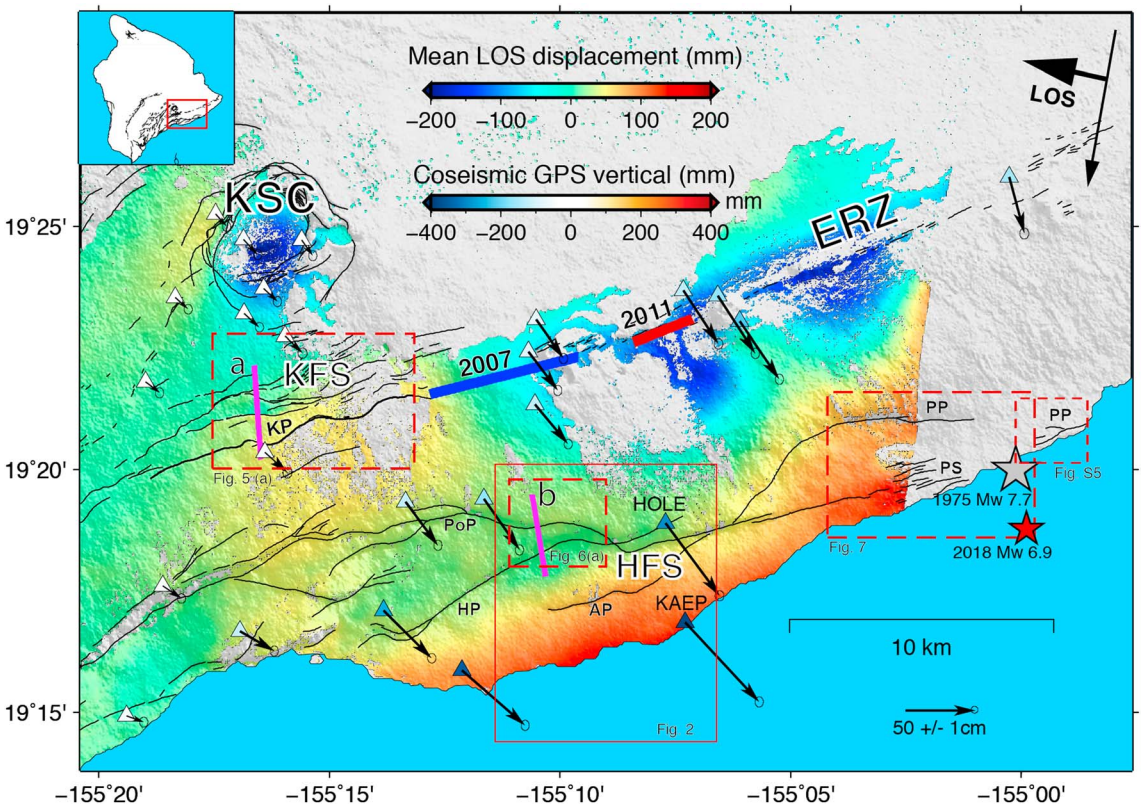

Figure 1. Map view of Kīlauea's south flank and normal fault systems (KSC = Kīlauea summit caldera; ERZ = East Rift Zone; KFS=Koa'e fault system; HFS=Hilina fault system). The gray and red stars represent the epicenters of the 1975 M7.7 Kalapana and 4 May 2018, M 6.9 earthquake, respectively. The black lines with black text labels denote the active fault traces mapped by U.S. Geological Survey (USGS; Cannon et al., 2007). KP= Kulanaokuaiki Pali; PoP=Poliokeawe Pali; HP=Hōlei Pali; AP='Āpua pali; PP=Palama pali; PS=Paliliu section. The red dashed boxes represent the areas with close-up phase examinations labeled with their respective figure numbers. The red solid box outlines the benchmark location map in Figure 2. The triangles represent the continuous Global Positioning System (GPS) stations in the study area. The symbol colors and arrows denote the vertical and horizontal displacements, respectively, due to the 2018 M 6.9 earthquake derived from 5-min GPS solutions (http://geodesy.unr.edu/news_items/20180505/us1000dyad.txt). The thick blue and red line segments show the approximate extent of the intrusions associated with the 2007 Father's Day and 2011 Kamoamoa eruptive events along the ERZ. The background color shows the mean line-of-sight (LOS) displacements due to the 2018 Kīlauea eruption-earthquake sequence derived from the stack of descending COSMO-Skymed (CSK, track D165) interferograms spanning the 2018 earthquake (see Figure S1 in the supporting information for the baseline plot). Positive values correspond to surface motion toward the satellite. Displacements along profiles a (crossing the KFS) and b (crossing the Poliokeawe and Hōlei Palis) are shown in Figures 5 and 6, respectively. Note that the interferometric synthetic aperture radar (InSAR) LOS displacements contain surface deformation due to the M6.9 earthquake on 4 May 2018 as well as magmatic activity during the approximately 1-month long observation period.

resurfaced by lava flows (Duffield, 1975; Podolsky & Roberts, 2008). The KFS has also hosted several historical dike intrusions suggesting that it represents a connecting structure between Kīlauea's two rift zones (Swanson et al., 2018). The KFS has been interpreted as a zone of localized extension and normal faulting that is activated by stresses generated by episodic dike intrusions in the two rift zones and the southward displacement of the south flank, including during major detachment earthquakes (Duffield, 1975; Swanson et al., 2018). Thus, the KFS grows by repeated episodes of injection of magma into the rifts, tearing the volcano apart as the south flank is forced away from the rifts (Duffield, 1975).

The HFS, located lower and further south on the flank, represents a zone of deformation about 5 km wide comprised of a series of en échelon, overstepping normal fault segments connected by relay ramps (Figure 1; Peacock & Parfitt, 2002). Individual Hilina scarps accommodate vertical offsets of up to 500 m (e.g., Lipman et al., 1985) and are often draped by young lava flows (Figure 2), providing some constraint on their slip history (Cannon & Bürgmann, 2001).

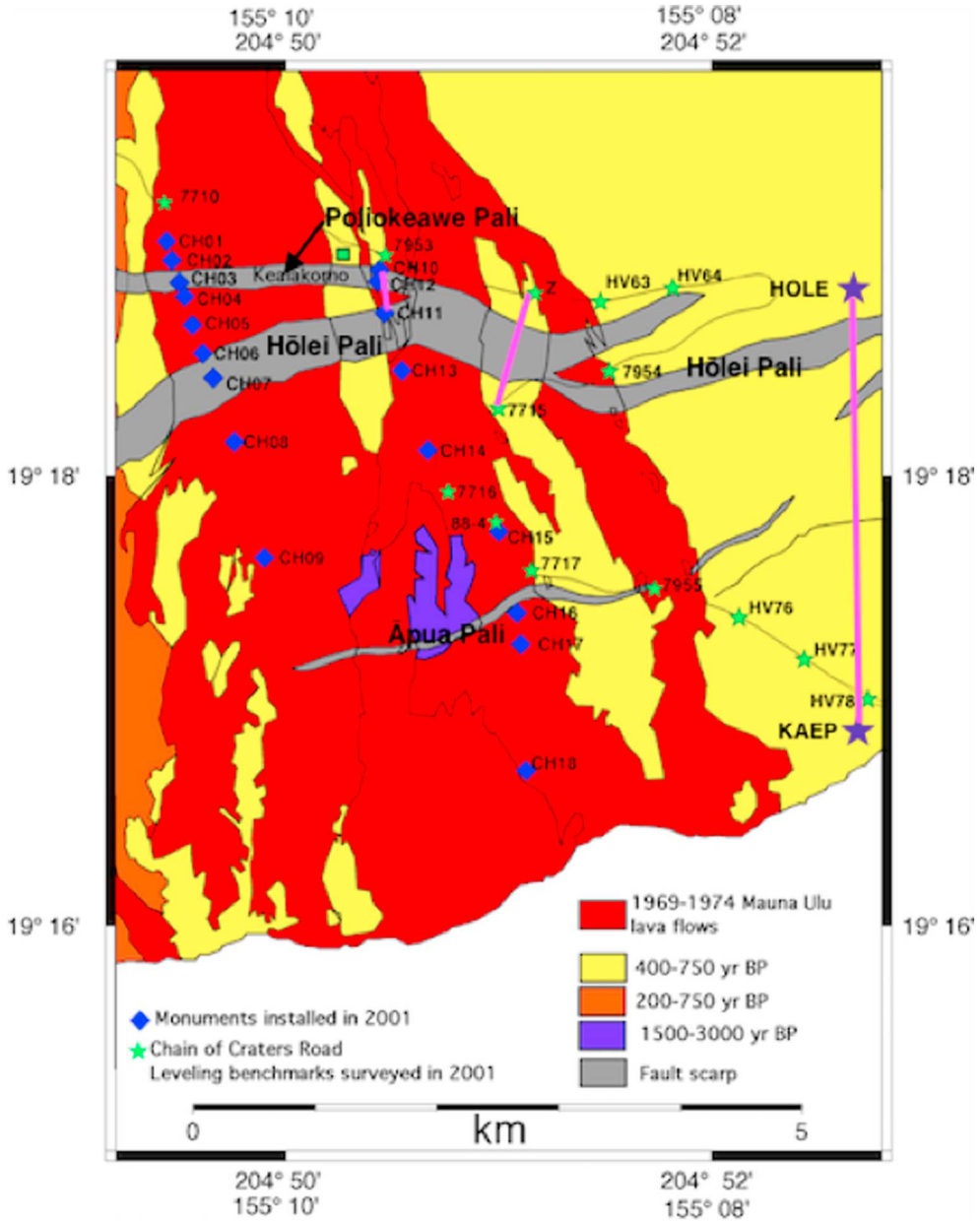

Figure 2. Close-up map of Global Positioning System (GPS) network across Hilina fault system (HFS; modified from Cannon et al., 2001). The colored polygons are lava flows with ages indicated in the legend. The grey bands outline the topographic fault scarps of the HFS. The green stars are Hawaiian Volcano Observatory (HVO) leveling benchmarks along the Chain of Craters road; the blue diamonds are benchmarks installed across the Poliokeawe, Hōlei, and ʻĀpua strands of the HFS in 2001. The magenta lines represent the location of the GPS baselines plotted in Figure 4. The green stars are HVO leveling benchmarks along the Chain of Craters road (referred to as "Hilina Road" in the text). The blue diamonds are benchmarks installed along two profiles ("Hilina West" and "Hilina East") across the Poliokeawe, Hōlei, and ʻĀpua strands of the HFS in 2011.

Although major historical earthquakes have all occurred on the primary detachment fault at the base of Kīlauea's edifice, some of the HFS normal faults are known to coseismically slip at the surface during such events (e.g., Cannon & Bürgmann, 2001) with potential small contributions by interseismic creep (Shirzaei et al., 2013). Associated with the 1975 earthquake, roughly 25 km of the HFS slipped with displacements of 1–3 m (Cannon et al., 2001; Lipman et al., 1985). Leveling, tilt, and trilateration data spanning the time of the 1975 event also show evidence of subsidence of the caldera due to magma withdrawal, and localized

subsidence was measured over the rift zones due to 3–5 m of rift-normal opening during or soon after the mainshock (Owen & Bürgmann, 2006). The geodetic measurements also indicate that significant horizontal extension (up to 2 m) and southward tilting occurred across the Koa'e fault system during the 1975 earthquake (Tilling et al., 1976).

There is uncertainty about the three-dimensional structure and origin of the HFS as well as its role in the volcano-tectonic activity of Kīlauea. One possibility, inferred from modeling of surface displacements due to earthquakes and slow slip events, paleomagnetic constraints on fault block rotation, and offshore seismic reflection profiles, represents the faults as listric landslide features that bottom out at 3- to 4-km depth (Cannon et al., 2001; Cervelli, Segall, Johnson et al., 2002; Morgan et al., 2003; Riley et al., 1999). Bathymetry data have confirmed the presence of prehistoric submarine landslide deposits around the Hawaiian Islands associated with the detachment of large sectors (Moore et al., 1994; Morgan et al., 2003). A competing model, inferred from seismic imaging and structural analysis, proposes that the HFS extends all the way to the basal detachment at a depth of 7–9 km (Denlinger & Okubo, 1995; Lipman et al., 1985; Okubo et al., 1997; Parfitt & Peacock, 2001). In contrast to the shallow geometry, a set of faults reaching the detachment might have more long-term stability, as the faults are buttressed by the weight of the entire flank.

Several authors have noted that the HFS faults likely have experienced no measurable slip since 1975 by comparing km-scale baselines across the faults (e.g., Delaney et al., 1998; Owen et al., 2000), while 2003–2010 InSAR data indicate the possibility of very modest (few millimeter) and episodic aseismic slip (Shirzaei et al., 2013). We present GPS measurements of a densely spaced profile of benchmarks that was established across a section of the HFS in 2001. The data reveal that between 2001 and 2017, there was no significant offset across several of the surface traces of the HFS that slipped in 1975.

The 4 May 2018, M6.9 earthquake, provides us with the opportunity to examine whether the event and associated magmatic activity triggered any slip in the HFS and KFS. Using InSAR, we show that modest slip of $\leq$10 mm occurred on two strands of the 1975 HFS surface rupture near the Hilina GPS survey network at approximately the time of the 4 May earthquake. A previously unmapped surface scarp is also observed near the easternmost section of the HFS, which produced surface deformation of over 20 cm. On the other hand, strands of the KFS slipped up to tens of centimeters in a series of discrete episodes during an ~3-month period of rapid Kīlauea summit deflation following the M6.9 earthquake.

2. Methods and Data

We analyze GPS data taken from closely spaced benchmarks that span one section of the HFS, including Poliokeawe Pali, Hōlei Pali, and ʻĀpua Pali and that we refer to as the Hilina survey network. Figure 2 shows the location of the benchmarks together with the individual fault scarps that the benchmarks traverse. The 1969–1974 Mauna Ulu lava flows drape the faults and were subsequently fractured in 1975 due to coseismic rupture (Cannon et al., 2001). We installed new benchmarks and collected initial GPS campaign measurements along two profiles in 2001 and 2003 ("Hilina East" starting at benchmark CH10 and "Hilina West" starting at benchmark CH01; blue diamonds in Figure 2). These were later supplemented by additional surveys by multiple groups under the oversight of the Hawaiian Volcano Observatory (HVO) between 2010 and 2017, as well as surveys of additional benchmarks along Chain of Craters Road ("Hilina Road" starting at benchmark BM79-503; green stars in Figure 2).

The initial occupations of the Hilina East (starting at benchmark CH10; Figure 2) and Hilina West (starting at benchmark CH01; Figure 2) lines were partly done as standard campaign GPS occupations lasting 13–15 hr or as approximately minute-long real-time kinematic surveys. After 2010, data were collected using Leica GPS500 kinematic GPS systems. One minute of dual-frequency data was collected at each benchmark, and the data were processed using the Leica GeoOffice software with reference stations taken from HVO's continuous GPS network. Surveys were done by multiple student groups, with the result that 11 surveys of the Hilina East line, 6 of the Hilina West line, and 19 surveys of the Hilina Road line were completed between 2010 and 2017. Not all surveys included all benchmarks of a given line.

In addition to the GPS data taken from a small section of the HFS, we examined C-band Sentinel-1 A/B and X-band COSMO-Skymed (CSK) interferograms that span the 2018 M 6.9 earthquake and the associated

major rift intrusion and eruption in an attempt to determine whether there was any coseismic deformation of the HFS and the KFS similar to what occurred in 1975. We processed the InSAR data with GMTSAR (Sandwell et al., 2011). Because of the relatively large orbit-separation baselines (see Figure S1 for the CSK baseline vs. time plot) and the intrinsically low radar reflectivity over vegetated parts of the island, image alignment with the built-in cross-correlation method often fails for CSK data. Therefore, similar to the processing of Sentinel-1 TOPS data, we aligned the CSK images to a single master for each track using the geometric alignment method. We first precisely map the footprint of each image acquisition on the ground using the information on SAR system's internal geometry, satellite's orbits, and external digital elevation model (DEM). A point-by-point offset map needed for the image alignment is then obtained by differencing the ground footprints (Wang et al., 2017; Xu et al., 2017). We used the 1-arc second (~30-m ground resolution) Shuttle Radar Topography Mission (SRTM) DEM for the geometrical alignment and removal of the topographic phase. We applied a low-pass Gaussian filtering with a 0.5 gain at a wavelength of 90 m to the real and imaginary parts of the original phase. A modified adaptive Goldstein filter (Goldstein & Werner, 1998) with $\alpha = 0.5$ was then applied to the low-pass filtered phase to obtain the final phase products.

3. Results and Analysis

3.1. 2001–2017 Deformation Across the HFS

In an effort to resolve slip across the HFS, we first computed GPS velocities for the stations in the Hilina survey network for two time periods, 2001–2010 and 2010–2017 (Figures 3a and 3b). Velocities in both maps are relative to the coastal station CH18 (depicted as a star in Figure 3). If the faults were slipping close to the surface, one would expect to see step increases in station velocities across successive fault blocks toward the south. However, both intervals are characterized by shortening, since stations to the north of CH18 appear to be moving toward that site. Shortening across the HFS is opposite to what would be expected for normal fault slip, in which the stations would be moving away from CH18. This contraction is partly a product of the major intrusive and eruptive events that occurred during this time period along Kīlauea's ERZ (Figure 1): the 2007 Father's Day (e.g., Montgomery-Brown et al., 2010), and the 2011 Kamoamoa (Lundgren et al., 2013) episodes. The HFS-spanning baseline between continuous GPS sites HOLE and KAEP (Figure 4a) clearly depicts south flank shortening associated with the two events, as evidenced by more southward motions at the station HOLE, compared to KAEP. Only for the period between the 2007 and 2011 rift intrusions and during 2014–2018 do we find evidence of extension across this section of the HFS (Figure 4a).

Although both Figures 3a and 3b indicate contraction during 2001–2010 and 2010–2017, the direction of shortening differs in the two time intervals: north-south during 2001–2010 and more westward in 2010–2017. The difference is further evidence that ERZ activity influences the contraction since the main zone of ERZ activity moved with respect to the GPS network over time. The 2007 event was located north of the stations (Montgomery-Brown et al., 2010; see Figure 1), while the 2011 event was further to the east (Lundgren et al., 2013). During neither period do we see a stepwise change in velocities across strands of the HFS.

To confirm that the average station velocities are representative of the station displacements during the two time periods, we also examined the time series of relative displacements of two short baselines spanning the HFS strands. Figures 4b and 4c show the north component of the baselines CH10-CH11 and Z-7715 (see magenta lines in Figure 2). Despite sparse temporal sampling, the data indicate little to no deformation across the baselines. However, the somewhat longer baseline Z-7715 shows a few cm of contraction associated with the 2011 Kamoamoa intrusion.

3.2. HFS and KFS Deformation Associated With the May 2018 M 6.9 Earthquake and Volcanic Activity

Given the increase in both volcanic and tectonic activity at Kīlauea from May to August of 2018, we seek to determine if there was slip along the Hilina and Koa'e faults during this episode. The 4 May 2018, M 6.9 earthquake, ruptured the basal detachment near the rupture zone of the M7.7 1975 event, during which the HFS and KFS experienced significant slip (Cannon et al., 2001; Lipman et al., 1985; Owen & Bürgmann, 2006; Swanson et al., 2018). To examine whether the 2018 M 6.9 earthquake also triggered slip on these fault systems, we inspected Sentinel-1 and CSK interferograms spanning the earthquake. In order to reduce the atmospheric noise, we first stacked the CSK interferograms with perpendicular orbit baselines

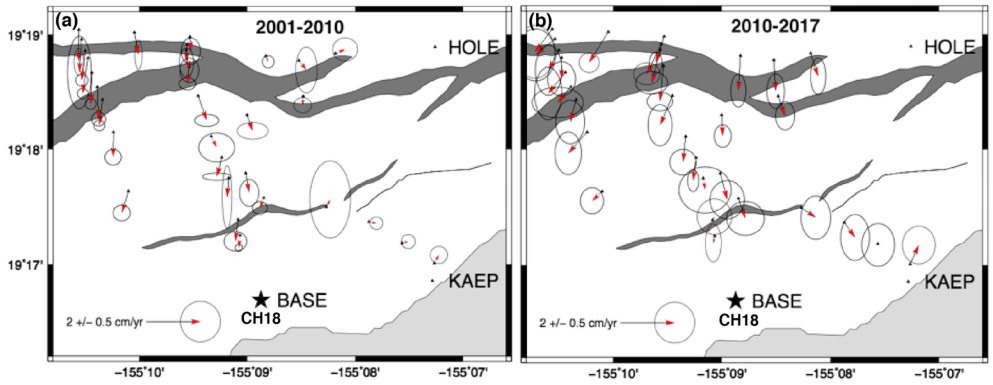

Figure 3. (a) 2001–2010 and (b) 2010–2017 average velocity maps for the benchmarks depicted in Figure 2. The coastal site, CH18, labeled BASE, is the base station to which all velocities are relative. The scale arrows in (a) and (b) are tipped with representative 67% confidence ellipses of 0.5 cm/year. Note that during both time periods, the south flank experienced shortening across the HFS. Note that confidence ellipses in (a) are scaled by a factor of three to account for added uncertainty due to the sparseness of measurements between 2001 and 2010 and the likely underestimate of the formal position uncertainties of individual campaign measurements.

<250 m (see Figure S1 for the baseline vs. time plots) to obtain the mean line-of-sight (LOS) displacements due to the May 2018 eruption-earthquake sequence. The mean LOS displacements of the CSK data from the descending track D165 are shown in Figure 1, spanning a roughly 1-month period including the earthquake. As a result of the rapid magma withdrawal from beneath the summit and upper ERZ, surface displacements near Kīlauea caldera and along the ERZ are characterized by significant range increase, corresponding to land subsidence. A large decrease in range (>10 cm) is found along much of the south coast, mainly due to the M 6.9 earthquake on 4 May 2018.

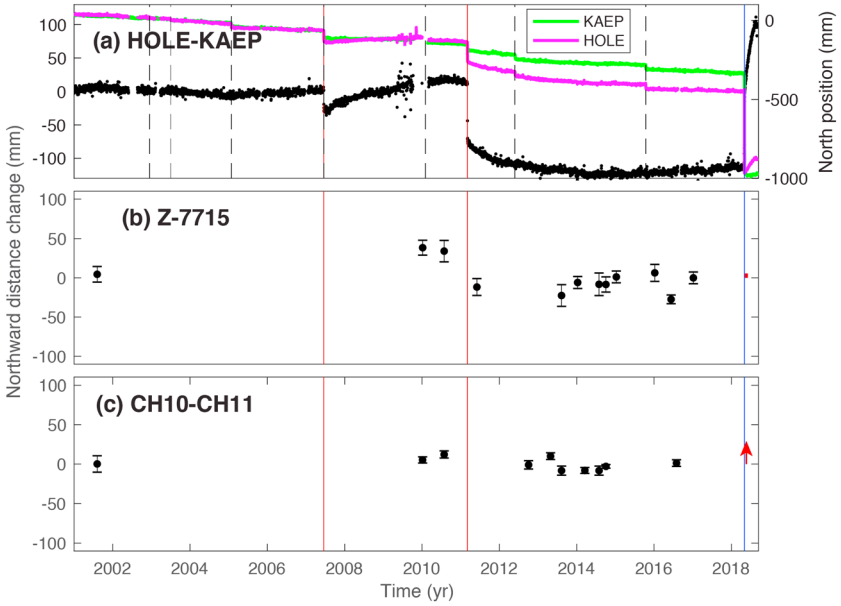

Figure 4. North component of baseline for pairs of (a) continuous and (b and c) campaign Global Positioning System stations across the Hilina fault system. The baseline changes are shown as black dots. The red vertical lines represent the time of the 2007 Father's Day and 2011 Kamoamoa eruptions. The blue vertical line represents the time of the 2018 M 6.9 earthquake. The individual time series of the stations HOLE and KAEP's north-component positions are also shown in (a) with colored lines (right axis). The black dashed vertical lines in (a) represent the times of slow slip events during the observation period (Montgomery-Brown et al., 2013; Montgomery-Brown et al., 2015). The red arrows in (b) and (c) represent the expected north-south extensions estimated from the coseismic InSAR results. See Figure 2 for the locations of the station pairs (depicted by pink lines).

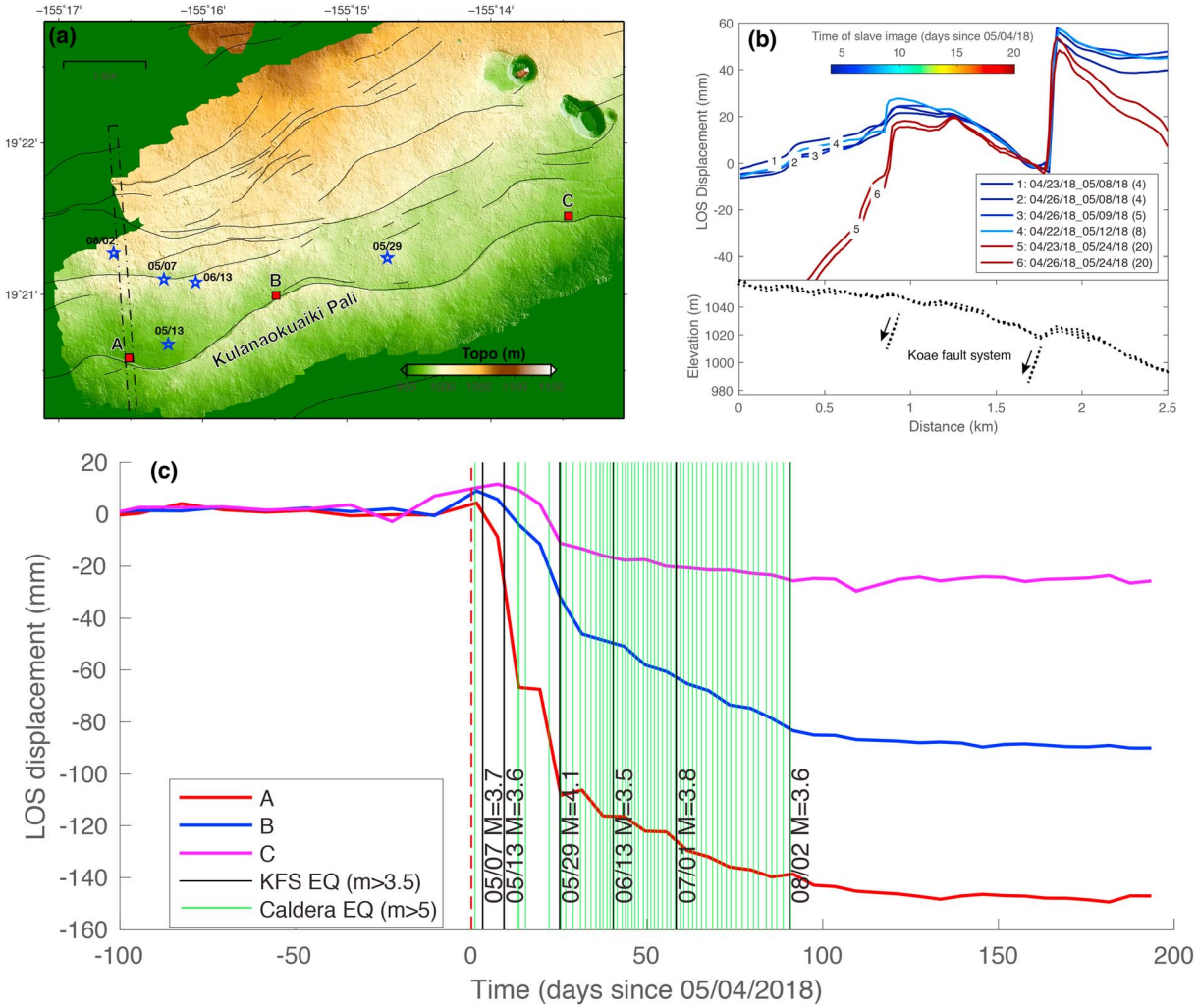

Figure 5. (a) Topography around the Koa'e fault system (KFS) derived from Lidar measurement (USGS, 2018). (b) Line-of-sight (LOS) displacements across the KFS derived from COSMO-Skymed (CSK) data from descending track D165. (c) Time series of relative displacements at different locations (A, B, and C in (a)) across the southernmost strand of the KFS derived from Sentinel-1 data from the descending track D87. At each epoch, the fault offset is computed by differencing the average values of LOS displacement within two circles of radius=120 meters across the fault. The red dashed line represents the time (UTC) of the M6.9 earthquake on 4 May 2018. The black lines represent the times (UTC) of M>3.5 earthquakes within the KFS shown by blue stars in (a). Note that the Sentinel-1 image on 29 May along the ascending track A124 was acquired ~1 hr after the M4.1 earthquake, which produced widespread surface deformation along the KFS. All depths of these events are <1 km. Since the KFS is thought to involve relatively shallow structures (e.g., <5 km), the proximity of these earthquakes to the KFS traces indicates that they are more likely to be associated with the KFS, rather than deep volcanic activities. The green lines denote the times of M>5 collapse events in the caldera area.

3.2.1. KFS Deformation Associated With 2018 Earthquake-Volcano Sequence

Close-up examination of the earthquake-spanning CSK interferograms reveals clear offsets in LOS displacements across the KFS (Figures S2–S4). The maximum offset in LOS displacements from the descending track D165 reaches >6 cm across the southernmost strand, Kulanaokuaiki Pali of the KFS, and gradually decays northward across multiple branches. Although all coseismic interferograms with the postearthquake image being acquired days after the M6.9 earthquake exhibit clear offsets across the KFS, coseismic interferograms ending with the first postearthquake image of 5 May 2018 (acquired ~18 hr after the earthquake) along the ascending track A10 does not show clear evidence of slip across the KFS (Figure S3). This implies that slip on the KFS was not directly triggered by the 4 May M6.9 earthquake. Instead, it is more likely related to the rapid subsidence of Kīlauea's summit region that initiated on 1 May, as a result of the magma withdrawal beneath the caldera to feed the eruptions along the lower ERZ.

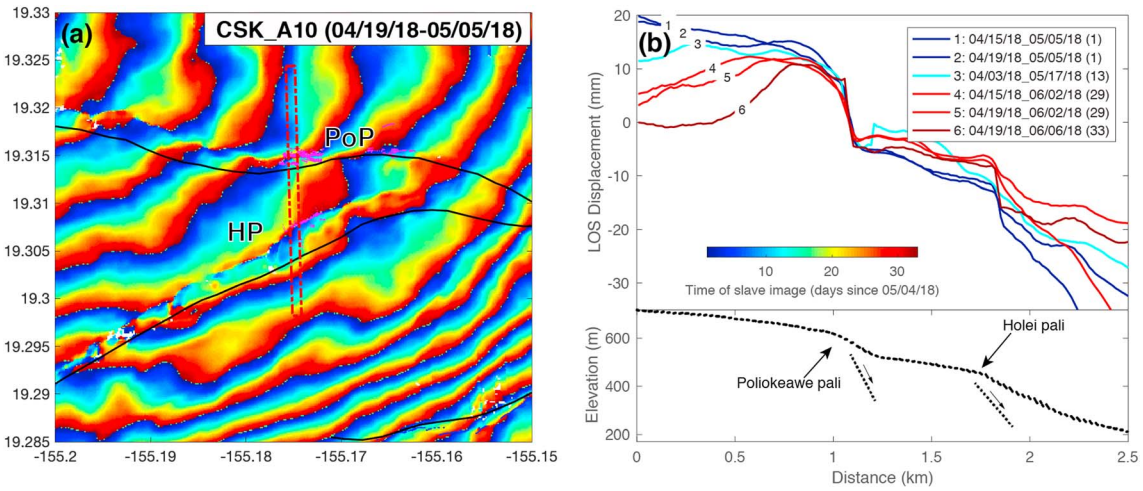

Figure 6. Triggered slip across the Hilina fault system. (a) Example interferometric phase of COSMO-Skymed data from the ascending track A10 at the Poliokeawe and Hōlei Palis of the Hilina fault system. Figure S4 presents additional interferograms showing coseismic offset across the Palis. The magenta lines indicate mapped locations of observed offsets triggered by the 1975 M7.7 Kalapana earthquake that were found in fresh 1974 Mauna Ulu lava flows (Cannon & Bürgmann, 2001). (b) Line-of-sight (LOS) displacements across the Poliokeawe and Hōlei Palis derived from COSMO-Skymed data of the ascending track A10. The line colors represent the time of the secondary image with respect to the M6.9 earthquake on 4 May 2018 (see Figure S1 for the baseline distribution). Numbers in parentheses in the legend denote the number of days between the slave image acquisition and the M6.9 earthquake.

Our analysis of InSAR time series of Sentinel-1 data shows that offsets on the Kulanaokuaiki Pali rapidly grew in concert with the continuing summit subsidence for at least 90 days (Figures 5c and S6). At a point close to the western end of the Kulanaokuaiki Pali (square A in Figure 5a), the cumulative LOS displacement from the Sentinel-1 descending track D87 reaches over 15 cm during ~200 days after the M6.9 earthquake. A significant portion of offset at this location, however, seems to occur mainly during a series of the m>3.5 shallow earthquakes in this area, although the displacement continued to increase until middle August, when the 2018 eruption episode finally stopped. Field observations in August to September 2018 reveal up to ~37-cm vertical offset at a point in the central section of the Kulanaokuaiki Pali (square B in Figure 5a; collected by Steve Lundblad and Don Swanson in August 2018). However, our InSAR time series at this location shows only moderate LOS displacement (~10 cm) during the entire observation period ending in December 2018 (blue line in Figure 5c). Assuming an incident angle of 38 degrees, the corresponding vertical displacement is 12.7 cm, still much smaller than the field observations. The smaller InSAR offset at this location may be partially attributed to the relatively low quality of the InSAR data in this area related to the thick forest and/or filtering in the data processing. The generally low radar phase correlation here may also cause unwrapping errors, leading to less consistent comparison between the InSAR and field observations. Further to east, at a location close to where the Kulanaokuaiki Pali crosses the Chains of Craters Road (square C in Figure 5a), the cumulative LOS displacement is 2–3 cm, which is in good agreement with the field observations collected by Steve Lundblad and Don Swanson in August 2018. Despite the noise, our InSAR data seem to suggest that the offset across the Kulanaokuaiki Pali decreases from west to east. The offsets across much of the Pali from point A to C suggest that the entire Kulanaokuaiki Pali moved during the 2018 earthquake-volcano sequence. However, the large subsidence signal around the caldera makes it difficult to accurately quantify how much slip occurred on individual northern strands of the KFS (Figure 5b and S6).

3.2.2. HFS Deformation Associated With 2018 Earthquake-Volcano Sequence

Data from CSK ascending track A10 reveal sharp offsets in LOS displacements of up to 10 mm across the Poliokeawe and Hōlei Palis, right where large coseismic offsets from the 1975 M 7.7 Kalapana earthquake were mapped by Cannon and Bürgmann (2001), shown by magenta lines in Figures 6a and S4. These offsets are probably not due to DEM error or atmospheric noise that may correlate with topography, as multiple, independent interferograms spanning the earthquakes all show these offsets, and those not spanning the earthquake do not have the offsets (Figure S4). The block-like offsets in the LOS displacement profiles (Figure 6b) suggest that they do not just represent superficial surface cracks but result from slip in the

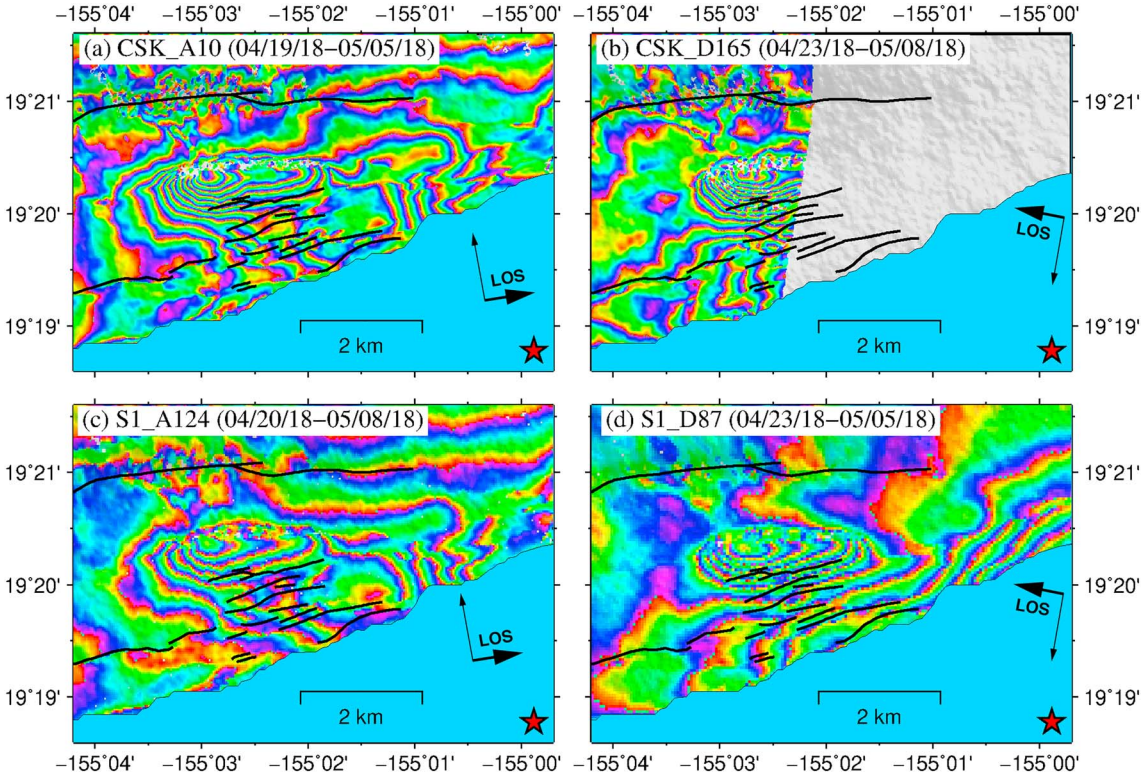

Figure 7. Surface deformation along the eastern Hilina fault system from COSMO-Skymed (CSK) and Sentinel 1 interferograms spanning the M 6.9 mainshock. (a–d) Wrapped phase of the coseismic interferograms (color ranges from −pi to pi) due to the coastal slump. Note the dense fringes at roughly the same locations of all four interferograms. One fringe corresponds to 1.55 and 2.8 cm of line-of-sight (LOS) displacement for CSK and Sentinel-1, respectively. The text in top-left corner of each panel shows the image acquisition information.

HFS from greater depth. Due to the dense spacing of the HFS branches and superimposed coseismic deformation field, we are not able to establish to what depth slip extends. The InSAR profiles across ʻĀpua Pali show no clear evidence of surface slip related to the 2018 M6.9 earthquake.

InSAR data from all satellite tracks spanning the time of the earthquake and subsequent months reveal substantial gradients in surface deformation near the eastern end of the HFS (Figure 7). No previously mapped faults are associated with this feature, although several mapped fault strands are present in the USGS fault database (Cannon & Bürgmann, 2001) both north and south of the high InSAR phase gradient. To better characterize the surface motion related to this previously unmapped structure, we combined the LOS displacements from both the ascending and descending tracks to decompose the east-west and vertical motions. In order to minimize the contribution of longer-wavelength surface deformation due to the basal slip of the M 6.9 earthquake and the magma intrusion (e.g., Figure 1), we select a reference point a few kilometer northeast of the structure (red circle in Figure 8), where the surface deformation due to the faulting is expected to be small. Due to the lack of observations along the azimuthal directions of the satellite tracks, current data do not constrain the north-south component of motion; thus, we focus on the vertical component, although significant southward motion is expected for a normal fault dipping to the south. For the coseismic deformation, both CSK and Sentinel-1 interferograms spanning the M6.9 earthquake with the shortest postseismic time spans of the respective satellite tracks are used in the decomposition. For the preseismic and postseismic deformation, we first solve for the time series of LOS displacements for the Sentinel-1 ascending A124 and descending D87 tracks over similar time intervals using Small Baseline Subset (SBAS) method (Berardino et al., 2002). We apply a Common-Scene-Stacking (CSS) method (Tymofyeyeva and Fialko, 2015; Wang & Fialko, 2018) to reduce the noises mostly due to the turbulent component of the atmospheric delays. The resulting cumulative LOS displacements of

the two Sentinel-1 tracks are then used to decompose for the vertical and horizontal motions during the respective time periods. We admit that the time differences in image acquisitions from different satellite tracks could affect the decomposition results. However, image acquisitions from the Sentinel-1 ascending track A124 and descending track D87 are only different by less than 3 days, and all the second images of interferograms used in the coseismic decomposition were acquired no later than 8 May. Compared to the deformation over the respective time periods, the effect due to time differences of image acquisitions is small, and thus ignored in the decomposition analysis.

In the interferograms spanning the mainshock, a normal-fault scarp indicated by steep InSAR phase gradients produced significant subsidence of up to ~20 cm (Figure 8b). CSK and Sentinel-1 InSAR observations over nearly 4 months after the 4 May 2018 earthquake reveal clear postearthquake deformation associated with this structure. Significant postseismic deformation is also found in a roughly east-west elongated zone ~2–3 km southeast of the coseismically activated normal fault scarp, along the Paliuli section of the HFS (Figure 8c), where only modest immediate coseismic deformation occurred.

Cooling and contraction of lava flows can cause detectable surface subsidence months to years after their emplacement (e.g., Bagnardi et al., 2016). Sentinel-1 observations from January to the end of April 2018 reveal up to 6-cm subsidence in the area of recent lava flows from Pu'u 'Ō'ō (Figure 8a). While the topography was altered by the lava accumulation, we note that such a large range change for Sentinel-1 interferometry with small orbit baselines is not likely to be due to the inaccuracy of the DEM. The relationship between DEM error and the corresponding range bias is given by

$$\Delta \mathrm{l} = \frac{R^{*}B_p}{\rho b \sin\theta}\Delta h$$

where R is the radius of the Earth, B_p is the perpendicular baseline, ρ is the range from the satellite to the ground, b is the orbital radius of the satellite, and θ is the radar incident angle. With appropriate values for Sentinel-1 (Bp<80 m), a 6-cm-range change corresponds to a DEM error >360 m, which is too large to be expected from the lava accumulation.

Compared to the coearthquake and postearthquake deformation in this area (Figures 8b and 8c), the preearthquake subsidence is well bounded by the recent lava emplacement, with a localized zone of subsidence just south of Pulama Pali and little deformation in the area of major coseismic and postseismic movement. Eruptions from Pu'u 'Ō'ō have stopped since the onset of the 2018 eruption sequence. The broader and larger coseismic and postseismic subsidence south of the preearthquake subsidence is thus not likely due to lava contraction. Instead, we argue that the coseismic and postseismic deformation primarily stem from normal faulting in this area.

4. Discussion

The south flank of Kīlauea is one of the most geologically active places in the world with significant spatial and temporal gradients in the pattern of deformation due to magma flow, slow slip events, and earthquakes, which can produce both favorable and unfavorable conditions for fault slip within the HFS. The 9-year data gap between the 2001 and 2010 GPS measurements limits our ability to assess temporally varying deformation across the HFS during this period. Although our velocity map for this period indicates contraction, this contraction was likely dominated by a single event: the 2007 Father's Day eruption (Montgomery-Brown et al., 2010). The HOLE-KAEP baseline, which spans the entire HFS, abruptly shortened at the times of the 2007 and 2011 rift eruptions and experienced several centimeter of extension between the two episodes (Figure 4a). There was little internal south flank deformation during other periods.

Our analysis of GPS-measured near-field displacements indicates that multiple strands along a central section of the HFS did not slip shallowly during the 2001–2017 period, a time mostly dominated by contraction across the south flank (Figures 3 and 4). However, these findings do not rule out the possibility of interseismic fault slip at other times or along other sections of the faults. For example, Shirzaei et al. (2013) used InSAR to suggest very small amounts of differential motion across a western section of the HFS to the

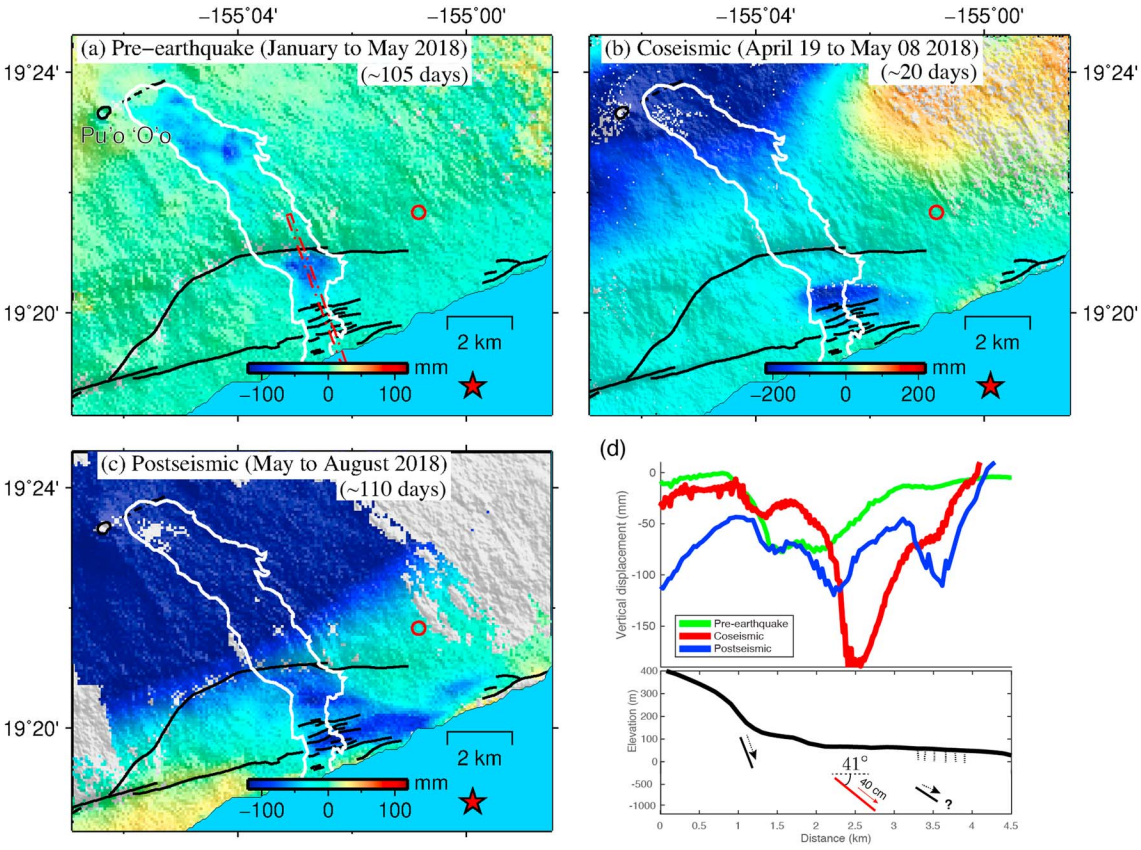

Figure 8. Vertical displacements along the eastern Hilina fault system from ascending and descending interferograms for (a) preearthquake period from early January 2018 to just before the M6.9 earthquake, (b) coseismic period (Figure 7), and (c) postseismic period from 5 May 2018 to the end of August 2018. The red circle in (a)–(c) represents the reference point for interferometric synthetic aperture radar time series analysis. The red star denotes the epicenter of the M6.9 earthquake. The white lines outline a flow from Pu'u 'Ō'ō flow field on March 2018 that started in June 2016. (d) Vertical displacements along a profile (red box in (a)) perpendicular to the fault lines. The solid and dashed lines beneath the topography profile sketch the possible subsurface fault geometry and approximate locations of mapped surface fault traces along the Paliliu section of the Hilina fault system, respectively, with the red line representing the preferred fault geometry from modeling of surface deformation due to the newly identified fault scarp.

west of the GPS network we examined, during the 2003–2010 period, but do not find resolvable offsets along the central HFS.

In contrast to the 2007 and 2011 intrusions, which led to contraction between HOLE and KAEP, the 2018 eruption-earthquake sequence resulted in substantial extension between the sites and across the HFS both due to the earthquake and the period of rift contraction during the lower ERZ eruption in May-August 2018. The north-south extension of the HOLE-KAEP baseline reached over 20 cm between May and August 2018. This recent south flank extension likely produced shear and normal stress changes that encouraged slip on the HFS.

The overall contraction of the south flank from 2001 to 2017 is similar to what was revealed by EDM measurements in the late 1960s (Swanson et al., 1976). Baseline changes across the HFS in both time periods are characterized by shortening during the interseismic period and extension during large earthquakes. The old EDM measurements also suggest that once significant contraction had accrued across the south flank, even relatively small events (earthquakes and intrusions) could trigger period of extension across the HFS (Swanson et al., 1976). Interseismic quiescence and triggered slip during large earthquakes thus seem to be unique features of the HFS on the south flank.

The 2018 M 6.9 earthquake triggered subcentimeter amounts of offset (Figures 6 and S4) along two sections of the HFS spanned by the Hilina survey network. These faults last ruptured nearly half a century ago during

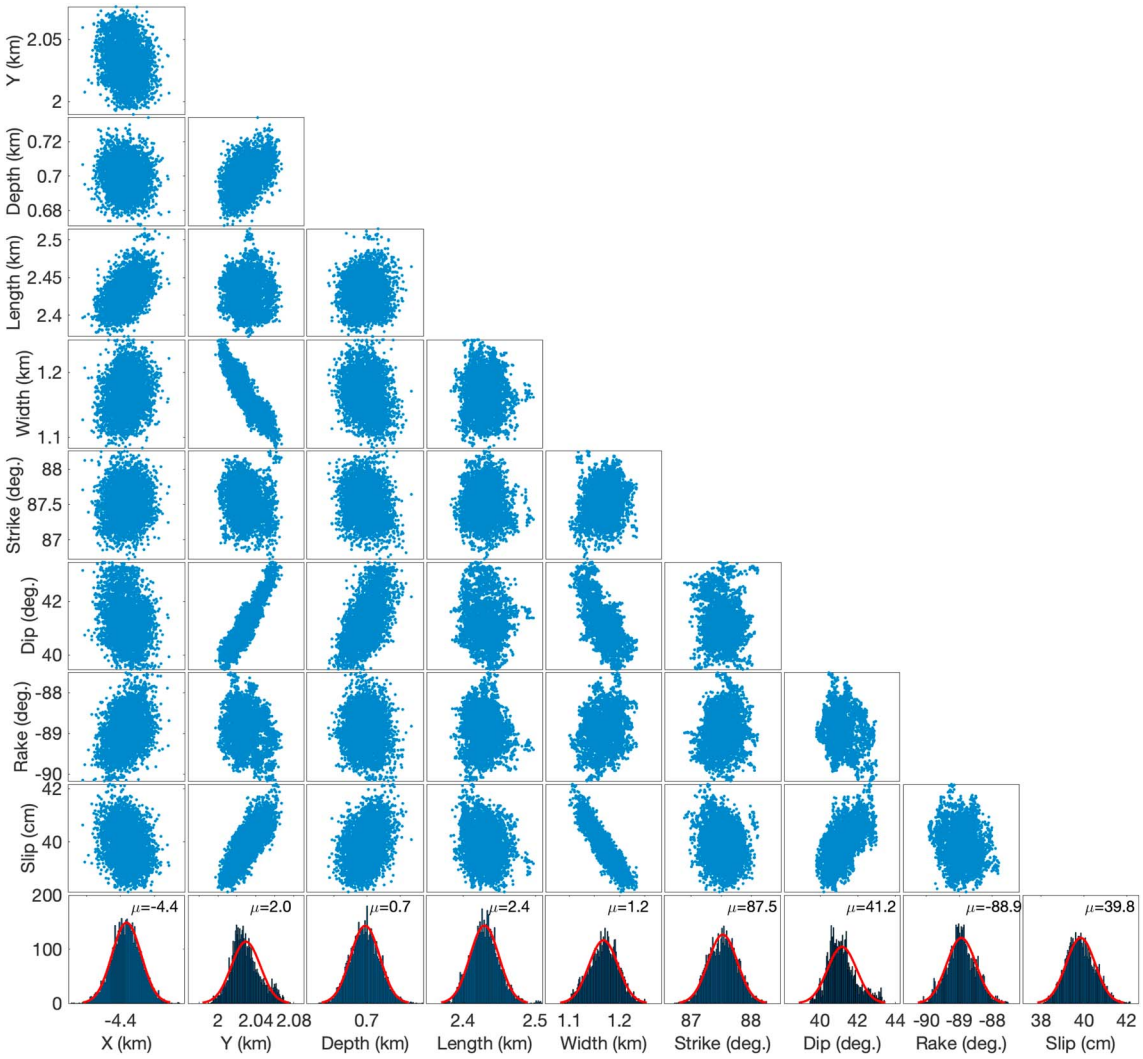

Figure 9. Model samples of the Bayesian inversion for the source of the new fault scarp. The bottom row shows the distributions of the respective model parameters, with the red curve in each panel representing the best fitting function of a normal distribution.

the much larger M 7.7 Kalapana event, when there were 1–2 m of horizontal and ~0.5 m of vertical displacements (Cannon & Bürgmann, 2001). The 1975 surface slip estimates were based on precisely measured offsets of 1974 lava flows. Adjacent 400- to 750-year-old flows are offset by several m, suggesting that 2–5 earthquakes of comparable magnitude would be needed to produce the older scarps (Cannon & Bürgmann, 2001). It is possible that the faults only experience substantial slip during major earthquakes above a certain magnitude threshold.

Closer to the epicenter of the 2018 event, we find modest offsets on multiple fractures in the Pulama segment of the easternmost HFS (Figure S5). Here surface faulting was also observed following the 1989 M6.1 décollement earthquake, when a few centimeter of subsidence and 15 cm of extensional ground surface cracking contributed additional seaward, suggesting that even moderate south flank earthquakes can cause localized failure along some sections of the HFS (Delaney et al., 1993). We note that two foreshocks (M5.1 and M5.4) occurred 2 and 1 hr before the mainshock, respectively. Due to their close proximity to the observed surface fractures (Figure 1), it is possible that they contributed to the ground deformation. If the HFS represents the headscarp of a relatively shallow landslide complex (e.g., Morgan et al., 2003), slip releasing gravitational potential may have been triggered by dynamic shaking, rather than in response to static stress changes on the faults.

While triggered slip along the existing major HFS strands appears to have been minor in 2018, we find evidence for normal faulting near the eastern end of the HFS away from previously mapped faults (Figures 7 and 8b). The largest surficial deformation feature associated with the 4 May 2018 earthquake consists of a localized zone of subsidence, bounded in the north by a sharp headscarp. This deformation occurs within and extends beyond lava flows emplaced during the preceding two years. There are multiple strands of the HFS to both the north and south of this feature (Cannon et al., 2007; black lines in Figure 7) that were mapped in >500-year-old lava (Holcomb, 1987). It is possible that the recent faulting represents the formation of a small, 2- to 3-km-long segment of the HFS, but much of this area is now covered by younger lava flows and it may be challenging to assess if this feature reactivated preexisting fractures.

To explore the subsurface geometry of this new fault scarp, we model the coseismic InSAR displacements associated with this feature, assuming that the observed deformation can be approximated by a normal fault with uniform slip along a rectangular fault patch. We calculate the Green's functions, relating unit slip to surface LOS displacement, using the solution of a rectangular dislocation in a homogeneous elastic half-space (Okada, 1985). We solve for the fault centroid location (x, y, z), dimension (length and with), geometry (strike and dip), and the slip magnitude and rake of the slip on the fault. We solve the problem in a Bayesian inversion framework, with the assumption of a uniform distribution of a priori probabilities for all model parameters. We assume a uniform variance of 2.25 cm^2 for all subsampled data points, and zero covariance between them. We sampled the model space using the *slice* sampling algorithm in MATLAB.

The distributions of model samples that yield high posterior probabilities are shown in Figure 9. The most likely model corresponds to a gently south-dipping (dip angle ~41°) fault patch of 2.4 km long by 1.2 km width with ~40-cm normal slip centered at a depth of 0.7 km. Given these parameters, the updip edge of the fault patch is estimated to be at a depth of ~300m, indicating that the fault likely did not reach to the surface. This is consistent with the lack of surface offset in the field. On 15 May 2019, we hiked out to the presumed fault trace inferred from InSAR to look for the potential surface offset associated with this fault scarp. While there were plenty of cracks vaguely strike in east-west direction, there was nothing conclusively related to faulting at a scale of kilometer. The preferred fault model predicts the surface deformation of both Sentinel-1 tracks reasonably well (Figure S7).

As described in the introduction, it is still unclear whether the HFS bottoms out at a relatively shallow depth of 3–4 km along a listric fault surface or it penetrates further deeper connecting to the basal detachment. If the newly formed fault scarp identified in this study is part of the HFS, the gentle dip angle (41°) and relatively shallow depth (less than 1 km) of slip concentration derived from the modeling above seem to be more consistent with the listric fault model that bottoms out at a relatively shallow depth. This is also suggested by the apparent southward migration of deformation during the postseismic period (Figure 8).

Near-field geodetic observations document that extension across the KFS occurred at an average rate of ~4.5 cm/year, during coseismic strains, rift intrusions, and also by aseismic fault creep, during the last five decades (Swanson et al., 2018). Historically, the KFS has been intruded, at least in part, by dikes during episodes in 1965, 1969, 1973, 1999, and 2007, which initiated from both the southwest rift zone and the ERZ (Duffield, 1975; Poland et al., 2014; Swanson et al., 2018, and references therein). In the 1965, 1999, and 2007 episodes, slip was documented along the eastern KFS by leveling surveys (Fiske & Koyanagi, 1968), InSAR (Cervelli, Segall, Amelung, et al., 2002), and field surveys (Montgomery-Brown et al., 2010). During the 2018 M6.9 earthquake, the KFS experienced moderate coseismic deformation. Subsequently, fault offsets accumulated as the earthquake rate on the KFS increased in response to summit subsidence (Figure 5). Larger increments of slip appear to be associated with shallow M>3.5 events in the KFS (Figure 5c). The shallow depth and timing relative to the eruption suggests that the KFS acted as part of the southern boundary of the subsiding summit caldera system.

5. Conclusions

The KFS and HFS represent the two major normal fault systems on Kīlauea's southern flank. Despite their prominence, neither their geometry nor their slip hazard potential has been fully constrained. Repeated GPS

surveys of a dense benchmark network across one section of the HFS in the 2001-2017 period reveal no evidence for shallow interseismic slip at that locality. Extension across the HFS was observed during the 2018 eruption-earthquake sequence, and centimeter-level slip was observed with InSAR on this section where surface slip triggered by the 1975 Kalapana earthquake exceeded 1 m. Interferograms spanning the earthquake also revealed a patch of normal-fault slip along the easternmost HFS near the M6.9 epicenter. A nearby 2- to 3-km-long scarp offset and associated subsidence zone of ~20 cm does not coincide with a previously mapped fault. Our observations support episodic sympathetic slip on the HFS associated with large-magnitude earthquakes. In contrast to the HFS, the KFS slips both steadily and episodically (Swanson et al., 2018). In 2018, the KFS experienced numerous discrete slip events in response to deflation at Kīlauea's summit, which was caused by large magma withdrawal feeding eruptions on the lower ERZ.

Acknowledgments
We acknowledge support by the UC Berkeley Larsen fund and the NASA ESI program (NNX16AL17G). Sentinel-1 data are copyright of European Space Agency (ESA) and archived and distributed by Alaska Satellite Facility (ASF). COSMO-Skymed data are copyright of the Italian Space Agency (ASI) and were provided courtesy of the Hawai'i Supersite. Field activities were conducted within Hawaii Volcanoes National Park and the authors are grateful to students from the University of Alaska, Fairbanks; South Dakota School of Mines and Technology; the Center for the Study of Active Volcanoes' International Training Course, and others for collecting kinematic GPS survey data on the Hilina Pali over many years. We thank Don Swanson and two anonymous reviewers for their comments and suggestions that helped improve this manuscript. The GPS velocities used in this study are provided in the supporting information online of this manuscript. CSK SAR data are available from the Italian Space Agency (ASI) via the Hawaiian Supersite (http://geo-gsnl.org/hawaiian-volcanoes-supersite/). The original Sentinel-1 data are downloaded from the Alaska Satellite Facility (www.asf.alaska.edu). Any use of trade, firm, or product names is for descriptive purposes only and does not imply endorsement by the U.S. Government.

References

Ando, M. (1979). The Hawaii earthquake of November 29, 1975: Low dip angle faulting due to forceful injection of magma. *Journal of Geophysical Research*, *84*(B13), 7616–7626. https://doi.org/10.1029/JB084iB13p07616

Bagnardi, M., González, P. J., & Hooper, A. (2016). High-resolution digital elevation model from tri-stereo Pleiades-1 satellite imagery for lava flow volume estimates at Fogo Volcano. *Geophysical Research Letters*, *43*, 6267–6275. http://doi.org/10.1002/2016GL069457

Berardino, P., Fornaro, G., Lanari, R., & Sansosti, E. (2002). A new algorithm for surface deformation monitoring based on small baseline differential SAR interferograms. *IEEE Transactions on Geoscience and Remote Sensing*, *40*(11), 2375–2383. https://doi.org/10.1109/TGRS.2002.803792

Borgia, A., Delaney, P. T., & Denlinger, R. P. (2000). Spreading volcanoes. *Annual Review of Earth and Planetary Sciences*, *28*(1), 539–570. https://doi.org/10.1146/annurev.earth.28.1.539

Brooks, B. A., Foster, J., Sandwell, D., Wolfe, C. J., Okubo, P., Poland, M., & Myer, D. (2008). Magmatically triggered slow slip at Kīlauea Volcano, Hawaii. *Science*, *321*(5893), 1177. https://doi.org/10.1126/science.1159007

Cannon, E., & Bürgmann, R. (2001). Prehistoric fault offsets of the Hilina fault system, south flank of Kīlauea volcano, Hawaii. *Journal of Geophysical Research*, *106*(B3), 4207–4219. https://doi.org/10.1029/2000JB900412

Cannon, E. C., Bürgmann, R., Crone, A. J., Machette, M. N., & Dart, R. L. (2007). Map and data for Quaternary faults and fault systems on the Island of Hawai'i. *U.S. Geological Survey Open-File Report*, 2007-1284 (http://pubs.usgs.gov/of/2007/1284/), 1-81.

Cannon, E. C., Bürgmann, R., & Owen, S. E. (2001). Shallow normal faulting and block rotation associated with the 1975 Kalapana earthquake, Kīlauea Volcano, Hawaii. *Bulletin of the Seismological Society of America*, *91*(6), 1553–1562. https://doi.org/10.1785/0120000072

Cervelli, P., Segall, P., Amelung, F., Garbeil, H., Meertens, C., Owen, S., et al. (2002). The 12 September 1999 Upper East Rift Zone dike intrusion at Kīlauea Volcano, Hawaii. *Journal of Geophysical Research*, *107*(B7), 2150. https://doi.org/10.1029/2001JB000602

Cervelli, P., Segall, P., Johnson, K., Lisowski, M., & Miklius, A. (2002). Sudden aseismic fault slip on the south flank of Kīlauea volcano. *Nature*, *415*(6875), 1014–1018. https://doi.org/10.1038/4151014a

Delaney, P. T., Denlinger, R. P., Lisowski, M., Miklius, A., Okubo, P. G., Okamura, A. T., & Sako, M. K. (1998). Volcanic spreading at Kīlauea, 1976-1996. *Journal of Geophysical Research*, *103*(B8), 18,003–18,023. https://doi.org/10.1029/98JB01665

Delaney, P. T., Fiske, R. S., Miklius, A., Okamura, A. T., & Sako, M. K. (1990). Deep magma body beneath the Summit and Rift Zones of Kīlauea Volcano, Hawaii. *Science*, *247*(4948), 1311–1316. https://doi.org/10.1126/science.247.4948.1311

Delaney, P. T., Miklius, A., Arnadottir, T., Okamura, A. T., & Sako, M. K. (1993). Motion of Kīlauea Volcano during sustained eruption from the Puu Oo and Kupaianaha vents, 1983-1991; supplemental information. *Journal of Geophysical Research*, *98*(B10), 17,801–17,820. https://doi.org/10.1029/93JB01819

Denlinger, R. P., & Okubo, P. (1995). Structure of the mobile south flank of Kīlauea Volcano. Hawaii. *Journal of Geophysical Research*, *100*(B12), 24,499–24,507. https://doi.org/10.1029/95JB01479

Dieterich, J. H. (1988). Growth and persistence of Hawaiian volcanic rift zones. *Journal of Geophysical Research*, *93*, 4258–4270. https://doi.org/10.1029/JB093iB05p04258

Duffield, W.A. (1975). Structure and origin of the Koae fault system, Kīlauea Volcano, Hawaii. *U.S. Geological Survey Professional Paper 856*, 12 p.

Fiske, R. S., & Koyanagi, R. Y. (1968). The December 1965 eruption of Kīlauea Volcano, Hawaii. *U.S. Geological Survey Professional Paper 607*, 21 p.

Goldstein, R. M., & Werner, C. L. (1998). Radar interferogram filtering for geophysical applications. *Geophysical Research Letters*, *25*(21), 4035–4038. https://doi.org/10.1029/1998GL900033

Holcomb, R. T. (1987). In R. Decker, T. L. Wright, & P. H. Stauffer (Eds.), *Eruptive history and long-term behavior of Kīlauea Volcano (Hawaii)*, *Professional Paper*, (Vol. 1350, pp. 261–350). Denver, CO: U.S. Geological Survey.

Lipman, P.W., Lockwood, J.P., Okamura, R.T., Swanson, D.A., & Yamashita, K.M. (1985). Ground deformation associated with the 1975 magnitude 7.2 earthquake and resulting changes in activity of Kīlauea Volcano, Hawaii. *U.S. Geological Survey Professional Paper 1276*.

Lundgren, P., Poland, M., Miklius, A., Orr, T., Yun, S.-H., Fielding, E., et al. (2013). Evolution of dike opening during the March 2011 Kamoamoa fissure eruption, Kīlauea Volcano, Hawai`i. *Journal of Geophysical Research: Solid Earth*, *118*, 897–914. https://doi.org/10.1002/jgrb.50108

Montgomery-Brown, E., Poland, M. P., & Miklius, A. (2015). Delicate balance of magmatic-tectonic interaction at Kīlauea Vocano, Hawai'i, Revealed from slow slip events. In R. Carey, V. Cayol, M. Poland, & D. Weis (Eds.), *Hawaiian Volcanoes: From Source to Surface*. (Chap. 13, pp. 269–288). Hoboken, NJ: John Wiley & Sons, Inc. https://doi.org/10.1002/9781118872079.ch13

Montgomery-Brown, E. K., Sinnett, D. K., Poland, M., Segall, P., Orr, T., Zebker, H., & Miklius, A. (2010). Geodetic evidence for en echelon dike emplacement and concurrent slow slip during the June 2007 intrusion and eruption at Kīlauea Volcano, Hawaii. *Journal of Geophysical Research*, *115*, B07405. https://doi.org/10.1029/2009JB006658

Montgomery-Brown, E. K., Thurber, C. H., Wolfe, C., & Okubo, P. (2013). Slow slip and tremor search at Kīlauea Volcano, Hawaii. *Geochemistry, Geophysics, Geosystems*, *14*, 367–384. https://doi.org/10.1002/ggge.20044

Moore, J. G., Normark, W. R., & Holcomb, R. T. (1994). Giant Hawaiian landslides. *Annual Review of Earth and Planetary Sciences*, *22*(1), 119–144. https://doi.org/10.1146/annurev.ea.22.050194.001003

Morgan, J. K., Moore, G. F., & Clague, D. A. (2003). Slope failure and volcanic spreading along the submarine south flank of Kīlauea Volcano, Hawaii. *Journal of Geophysical Research*, *108*(B9), 2415. https://doi.org/10.1029/2003JB002411

Neal, C. A., Brantley, S. R., Antolik, L., Babb, J. L., Burgess, M., Calles, K., et al. (2018). The 2018 rift eruption and summit collapse of Kīlauea Volcano. *Science*, *363*(6425), 367–374. https://doi.org/10.1126/science.aav7046

Okada, Y. (1985). Surface deformation due to shear and tensile faults in a half-space. *Bulletin of the Seismological Society of America*, *75*(4), 1135–1154

Okubo, P. G., Benz, H. M., & Chouet, B. A. (1997). Imaging the crustal magma sources beneath Mauna Loa and Kīlauea Volcanoes, Hawaii. *Geology*, *25*(10), 867–870. https://doi.org/10.1130/0091-7613(1997)025<0867:ITCMSB>2.3.CO;2

Owen, S., Segall, P., Freymueller, J., Miklius, A., Denlinger, R., Árnadóttir, T., et al. (1995). Rapid deformation of the south flank of Kilauea Volcano, Hawaii. *Science*, *267*(5202), 1328–1332. https://doi.org/10.1126/science.267.5202.1328

Owen, S., Segall, P., Lisowski, M., Miklius, A., Denlinger, R., & Sako, M. (2000). Rapid deformation of Kīlauea Volcano: Global positioning system measurements between 1990 and 1996. *Journal of Geophysical Research*, *105*(B8), 18,983–18,998. https://doi.org/10.1029/2000JB900109

Owen, S. E., & Bürgmann, R. (2006). An increment of volcano collapse: Kinematics of the 1975 Kalapana, Hawaii, earthquake. *Journal of Volcanology and Geothermal Research*, *150*(1-3), 163–185. https://doi.org/10.1016/j.jvolgeores.2005.07.012

Parfitt, E. A., & Peacock, D. C. P. (2001). Faulting in the South Flank of Kīlauea Volcano, Hawai'i. *Journal of Volcanology and Geothermal Research*, *106*(3-4), 265–284. https://doi.org/10.1016/S0377-0273(00)00247-X

Peacock, D. C. P., & Parfitt, E. A. (2002). Active relay ramps and normal fault propagation on Kilauea Volcano, Hawaii. *Journal of Structural Geology*, *24*(4), 729–742. https://doi.org/10.1016/s0191-8141(01)00109-2

Podolsky, M. W., & Roberts, G. P. (2008). Growth of the volcano-flank Koa'e fault system, Hawaii. *Journal of Structural Geology*, *30*(10), 1254–1263. https://doi.org/10.1016/j.jsg.2008.06.006

Poland, M. P., Miklius, A., & Montgomery-Brown, E. K. (2014). Magma Supply, Storage, and Transport at Shield-Stage Hawaiian Volcanoes. In M. Poland, T. J. Takahashi, & C. M. Landowski (Eds.), *Characteristics of Hawaiian volcanoes*, *Professional Paper* (pp. 179–234). Denver: U.S. Geological Survey. https://doi.org/10.3133/pp1801

Riley, C. M., Diehl, J. F., Kirschvink, J. L., & Ripperdan, R. L. (1999). Paleomagnetic constraints on fault motion in the Hilina Fault System, south flank of Kilauea Volcano, Hawaii. *Journal of Volcanology and Geothermal Research*, *94*(1–4), 233–249. https://doi.org/10.1016/s0377-0273(99)00105-5

Sandwell, D., Mellors, R., Tong, X., Wei, M., & Wessel, P. (2011). Open radar interferometry software for mapping surface deformation. *Eos, Transactions of the American Geophysical Union*, *92*(28), 234. https://doi.org/10.1029/2011EO280002

Shirzaei, M., Bürgmann, R., Foster, J., Walter, T. R., & Brooks, B. A. (2013). Aseismic deformation across the Hilina fault system, Hawaii, revealed by wavelet analysis of InSAR and GPS time series. *Earth and Planetary Science Letters*, *376*, 12–19. https://doi.org/10.1016/j.epsl.2013.06.011

Swanson, D. A., Duffield, W. A., & Fiske, R. S. (1976). Displacement of the south flank of Kīlauea Volcano: The result of forceful intrusion of magma into the rift zones. *U.S. Geological Survey Professional Paper 963*.

Swanson, D. A., Fiske, R. S., Thornber, C. R., & Poland, M. P. (2018). Dikes in the Koa'e fault system, and the Koa'e-east rift zone structural grain at Kīlauea Volcano, Hawai'i. In M. Poland, M. O. Garcia, V. E. Camp, & A. Grunder (Eds.), *field volcanology: A tribute to the distinguished career of Don Swanson*, *Professional Paper*, (Vol. 538). Denver: U.S. Geological Survey. https://doi.org/10.1130/SPE538

Tilling, R. I., Koyanagi, R. Y., Lipman, P. W., Kockwood, J. P., Moore, J. G., Swanson, D. A. (1976). Earthquake and related atastropic events, Island of Hawaii, November 29, 1975: A Preliminary Report, U.S. Geological Survey Circular, 740.

Tymofyeyeva, E., & Fialko, Y. (2015). Mitigation of atmospheric phase delays in InSAR data, with application to the eastern California shear zone. *Journal of Geophysical Research: Solid Earth*, *120*, 5952–5963. https://doi.org/10.1002/2015JB011886

U.S. Geological Survey (2018). Kīlauea Volcano, HI (June 2018) Acquisition airborne lidar survey. U.S. Geological Survey (USGS) in collaboration with GEO1, Windward Aviation, Quantum Spatial, and Cold Regions Research and Engineering Laboratory, https://doi.org/10.5069/G98K7718 (distributed by OpenTopography; also available at https://kilauealidar.com); Survey Date: 06/01/2018-06/15/2018; Publication Date: 07/06/2018 (>10 billion points)

Wang, K., & Fialko, Y. (2018). Observations and modeling of coseismic and postseismic deformation due to the 2015 M w7.8 Gorkha (Nepal) Earthquake. *Journal of Geophysical Research: Solid Earth*, *123*, 761–779. https://doi.org/10.1002/2017JB014620

Wang, K., Xu, X., & Fialko, Y. (2017). Improving burst alignment in TOPS interferometry with bivariate enhanced spectral diversity. *IEEE Geoscience and Remote Sensing Letters*, *14*(12), 2423–2427. https://doi.org/10.1109/LGRS.2017.2767575

Wyss, M. (1988). A proposed source model for the great Kau, Hawaii, earthquake of 1868. *Bulletin of the Seismological Society of America*, *78*, 1450–1462.

Xu, X., Sandwell, D. T., Tymofyeyeva, E., González-Ortega, A., & Tong, X. (2017). Tectonic and anthropogenic deformation at the Cerro Prieto geothermal step-over revealed by Sentinel-1A InSAR. *IEEE Transactions on Geoscience and Remote Sensing*, *55*(9), 5284–5292. https://doi.org/10.1109/TGRS.2017.2704593